



This is a repository copy of *Comparison of rainfall microphysics characteristics derived by numerical weather prediction modelling and dual-frequency precipitation radar*.

White Rose Research Online URL for this paper:
<https://eprints.whiterose.ac.uk/174748/>

Version: Published Version

Article:

Zhu, J., Zhang, S., Yang, Q. et al. (3 more authors) (2021) Comparison of rainfall microphysics characteristics derived by numerical weather prediction modelling and dual-frequency precipitation radar. *Meteorological Applications*, 28 (3). e2000. ISSN 1350-4827

<https://doi.org/10.1002/met.2000>

Reuse

This article is distributed under the terms of the Creative Commons Attribution-NonCommercial-NoDerivs (CC BY-NC-ND) licence. This licence only allows you to download this work and share it with others as long as you credit the authors, but you can't change the article in any way or use it commercially. More information and the full terms of the licence here: <https://creativecommons.org/licenses/>

Takedown


If you consider content in White Rose Research Online to be in breach of UK law, please notify us by emailing eprints@whiterose.ac.uk including the URL of the record and the reason for the withdrawal request.



eprints@whiterose.ac.uk
<https://eprints.whiterose.ac.uk/>

RESEARCH ARTICLE

Comparison of rainfall microphysics characteristics derived by numerical weather prediction modelling and dual-frequency precipitation radar

Jingxuan Zhu¹ | Shuliang Zhang¹ | Qiqi Yang¹ | Qi Shen¹ | Lu Zhuo^{2,3} | Qiang Dai¹ 

¹Key Laboratory of VGE of Ministry of Education, Nanjing Normal University, Nanjing, China

²Department of Civil and Structural Engineering, University of Sheffield, Sheffield, UK

³Department of Civil Engineering, University of Bristol, Bristol, UK

Correspondence

Qiqi Yang, Key Laboratory of VGE of Ministry of Education, Nanjing Normal University, Nanjing, China.
Email: yangqiqi_gis@163.com

Funding information

National Key R&D Program of China, Grant/Award Numbers: 2018YFB0505500, 2018YFB0505502; National Natural Science Foundation of China, Grant/Award Numbers: 41871299, 41771424, 42071364

Abstract

The understanding of large-scale rainfall microphysical characteristics plays a significant role in meteorology, hydrology and natural hazards managements. Traditional instruments for estimating raindrop size distribution (DSD), including disdrometers and ground dual-polarization radars, are available only in limited areas. However, the development of space-based radars and mesoscale numerical weather prediction models would allow for DSD estimation on a large scale. This study investigated the performance of the weather research and forecasting (WRF) model and the global precipitation measurement mission (GPM) dual-frequency precipitation radar for DSD retrieval under different conditions. The DSD parameters (D_m and N_w), rain rate (R), rainfall kinetic energy (KE) and radar reflectivity (Z) were estimated in Chilbolton, United Kingdom, by using long-term disdrometer observations for validation. The rainfall kinetic energy–rain rate (KE – R) and radar reflectivity–rain rate (Z – R) relationships were explored using a disdrometer, the WRF model and GPM. It was found that the DSD parameter distribution trends of the three approaches are similar although the WRF model has larger D_m and smaller N_w values. In terms of the rainfall microphysical relationship, GPM performs better when both Ku- and Ka-band precipitation radars (KuPR and KaPR) observe precipitation simultaneously ($R > 0.5 \text{ mm h}^{-1}$), while the WRF model shows high accuracy in light rain ($R < 0.5 \text{ mm h}^{-1}$). The fusion of GPM and WRF model is recommended for the improved understanding of rainfall microphysical characteristics in ungauged areas.

KEYWORDS

GPM, raindrop size distribution, rainfall, rainfall kinetic energy, weather radar, WRF

1 | INTRODUCTION

Raindrop size distribution (DSD), defined as the probability density function of raindrop size, is an important

statistical characteristic used to reflect raindrop microphysics (Ulbrich, 1983). The DSD spectra play a crucial role in a variety of environmental applications such as precipitation estimation, remote sensing observations,

This is an open access article under the terms of the Creative Commons Attribution-NonCommercial-NoDerivs License, which permits use and distribution in any medium, provided the original work is properly cited, the use is non-commercial and no modifications or adaptations are made.

© 2021 The Authors. Meteorological Applications published by John Wiley & Sons Ltd on behalf of the Royal Meteorological Society.

radio communications, cloud microphysics investigation and soil erosion driven by rainfall (Jameson & Kostinski, 2001b; Kirankumar et al., 2008; Tokay et al., 2013). A good knowledge of DSD and its spatial-temporal variability within precipitation systems is vital to hydrology, meteorology and natural hazards (Chapon et al., 2008; Jaffrain et al., 2011; Uijlenhoet et al., 2003).

A range of research fields such as quantitative precipitation estimation (QPE) and soil erosion assessment require spatial DSD and microphysical characteristics data. Two empirical relationships are commonly used to bridge primitive rainfall microphysics observations and practical applications: the rainfall kinetic energy (KE)-rain rate (R) relationship (KE - R) and the radar reflectivity (Z)-rain rate relationship (Z - R). The KE - R relationship is an essential factor in soil erosion assessment to describe the splash impact energy of raindrops on soil particles (Angulo-Martínez et al., 2016; Kinnell, 2005; Renard, 1997; Wang et al., 2014; Wischmeier & Smith, 1978). It is not stationary across space and time and relies on the characteristics of DSD influenced by various geographical and meteorological factors (Van Dijk et al., 2002). The Z - R relationship under different environments (e.g. storm type, temperature, horizontal wind and aerosol effects) is the foundation of radar remote sensing and fully depends on dynamic DSD (Dai et al., 2019; Jameson & Kostinski, 2001a; Ji et al., 2019).

Ground-based disdrometers (electromechanical, acoustic and optical types) are traditionally used to measure DSD; these approaches collect DSD spectra by converting the signal generated by the falling drop and then deriving the parameters of model DSDs with limited spatial representability for the surrounding area (Angulo-Martínez et al., 2012; Angulo-Martínez et al., 2016; Jaffrain et al., 2011; Petan et al., 2010), owing to the spatial similarity of geographic configuration (Lü et al., 2019; Zhu et al., 2018). Considering that DSDs measured by disdrometers are only point-based, DSD must be obtained through large-scale raindrop microphysics measurements or simulations. A ground dual-polarimetric radar can also be used to derive DSD, which exhibits a circular domain with a radius of up to 200 km, by using radar signatures such as differential reflectivity and specific differential phase shift (Brandes et al., 2004; Bringi et al., 2003; Dai et al., 2019; Gorgucci et al., 2002).

Unlike ground dual-polarimetric radars that are available only in limited areas (Prigent, 2010), space-based radars can help measure DSD on a large scale. For example, the space-borne dual-frequency precipitation radar (DPR) containing the Ku-band (13.6 GHz) and Ka-band (35.5 GHz) on the global precipitation measurement mission (GPM) core satellite, which affords scan swaths of 245 and 120 km, allows researchers to estimate the 3D

spatial distribution of hydrometeors (Iguchi et al., 2018). DPR can estimate DSDs with an approximate coverage of up to 65° latitude by using wave dual-wavelength algorithms. Dual-frequency radar techniques usually utilize a differential frequency ratio within a 120 km inner swath as well as radar reflectivity at lower frequencies to estimate the DSD parameters (typically using a gamma distribution) and subsequently derive the rain rate (Liao et al., 2014; Mardiana et al., 2004; Meneghini et al., 1997; Rose & Chandrasekar, 2006; Seto et al., 2013; Seto & Iguchi, 2015).

In addition to the direct measurement of DSD parameters, the mesoscale numerical weather prediction (NWP) model is a promising method for interpreting the DSD variation on a large scale. NWP models, such as the weather research and forecasting (WRF) model, can be used to simultaneously derive DSD parameters in 3D spatial fields through microphysical cloud process simulation and the evolution of particle size distribution prediction based on computationally feasible parameterization schemes (Brown et al., 2016). Numerous options are provided by the WRF model for cloud microphysical schemes with different DSD models and parameter settings (Han et al., 2013). DSD on the ground can be derived from the WRF model by considering various hydrometeor types, physical processes and degrees of freedom in hydrometeor size distributions (Brown et al., 2016; Yang et al., 2019). The possible sensitivity associated with the retrieval of DSD parameters by WRF model has been investigated in recent studies (Khain et al., 2016; Planche et al., 2019; Yang et al., 2019). The WRF model can run with the initial and boundary conditions taken from global reanalysis datasets, such as the European Centre for Medium-range Weather Forecasts (ECMWF) and the National Centers for Environmental Prediction. In other words, WRF-derived DSD can be obtained for any given area with fine spatial and temporal resolutions.

GPM and WRF model can derive large-scale DSD, but their accuracy evaluation and verification are insufficient at present and it is not clear which is more suitable for practical applications in ungauged areas. The performance of DSD estimation may vary under different conditions, such as land cover, climate regime and storm type. Therefore, this study comprehensively compares the DSD retrieval performance of ground-based disdrometer with the GPM DPR and WRF model to provide a new perspective for using high-precision data fusion with the aim of DSD product generation on a large scale. The KE - R and Z - R relationships were established using all three approaches to provide insights into the use of DSD for rainfall erosivity estimation and accurate precipitation forecasting.

2 | MATERIALS

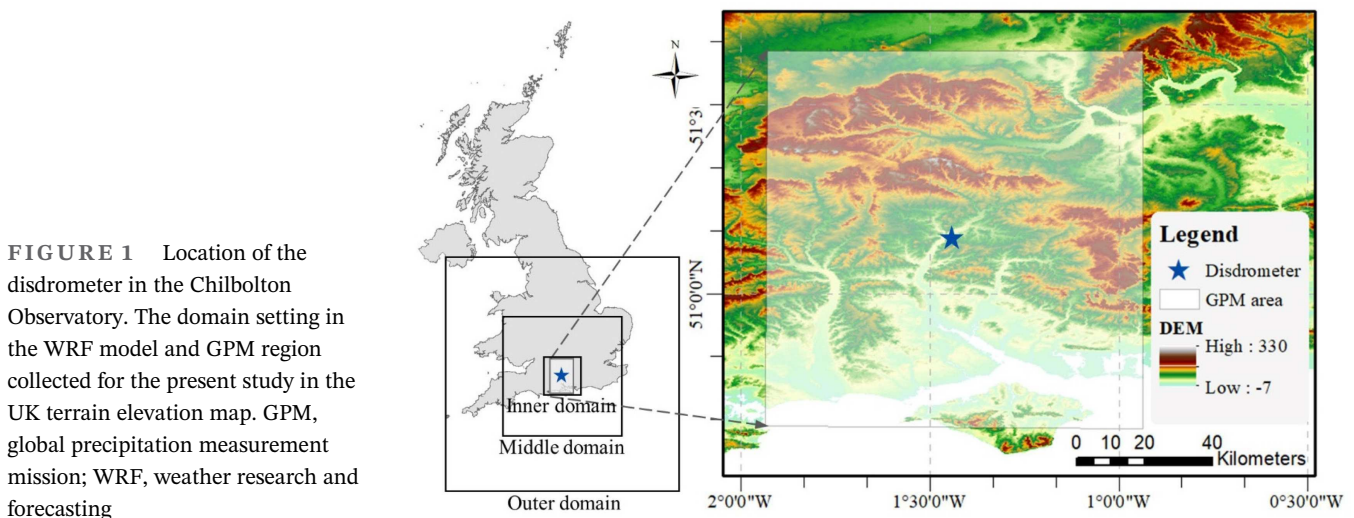
Ground-based disdrometer measurements of point DSD have been widely used for validation of rainfall retrieval by radar or NWP models. A disdrometer works by counting individual raindrops and measuring their size. The sensor consists of an electromechanical unit and a feedback amplifier housed in a cylindrical case (Islam et al., 2012). We used data from an impact-type JWD installed in the Chilbolton Observatory ($51^{\circ}08'N$, $01^{\circ}26'W$; Figure 1), which records the number of raindrops striking a 50 cm^2 sensor area with 127 bins of size from 0.3 to 5.0 mm. Chilbolton experiences a temperate maritime climate. The DSD data have been sampled and recorded in a 50 cm^2 area every 10 s from April 2003. The data collected by the British Atmospheric Data Centre can be retrieved online (<http://data.ceda.ac.uk/badc>). In this study, the 10-s measurement data during the entire 4 years (2014–2017) were averaged over a 1-min period to filter time variation, thereby avoiding the counting of fluctuations for a short period or smoothing the actual physical variation for a long period (Islam et al., 2012; Montopoli et al., 2008; Song et al., 2017).

The GPM DPR level-2 (L2) product (version 6), which covered the period from April 2014 to December 2019, was used to investigate the radar-derived DSD. The DPR L2 product consists of six datasets generated from basic, unprocessed and primary instrument data. The major improvement of GPM DPR compared with its predecessor (a precipitation radar [PR] of the Tropical Rainfall Measuring Mission) is the dual-frequency algorithm based on dual-wavelength data measured by the Ku- and Ka-band precipitation radars (KuPR and KaPR). Compared with PR, DPR increases sensitivity, facilitates the distinction between rain and snow and provides DSD information (Iguchi et al., 2018). Here, only reflectivity in the inner Ku swath pixels, which were obtained by

simultaneously using the Ku- and Ka-bands, could be retrieved by the dual-frequency (DF) algorithm; others were calculated from single-frequency (SF) retrieval.

The normal swath (NS) product in the DPR level-2A product (2ADPR) combines the DF products of the inner swath with the SF Ku-band products from the outer swath. The Ku-band SF estimates have been corrected by applying the DSD database derived from DF pixels. Vertical sampling echoes for DPR NS cover 176 bins from the ellipsoid to a height of 19 km above sea level, with the aim of obtaining 3D information. This study mainly uses the data of surface DSD parameters, including the mass-weighted mean drop diameter (D_m) and normalized intercept parameter (N_w) of the 2ADPR NS dataset. The 2ADPR data were obtained from the NASA GPM website (<https://pmm.nasa.gov/data-access/downloads/gpm>) by using approximately 16 files per day; this website has been archived in a Version 5 Hierarchical Data Format (HDF5) file for each orbit.

The ERA-Interim data provided by the ECMWF were selected to run the WRF model. ERA-Interim includes global atmospheric reanalysis data from January 1979 to the present day; it is considered an ambitious reanalysis project and an important atmospheric data source for scientific research (Dee et al., 2011). It uses the 4D variational with 6- and 12-h cycling to assimilate data, such as wind, temperature and humidity at different configurations (Mooney et al., 2011; Simmons, 2006). ERA-Interim provides a robust reanalysis system, while contributing to difficult data assimilation and the improvement of technical aspects associated with reanalysis products (Dee et al., 2011). The dataset is available at <http://apps.ecmwf.int/datasets>; it exhibits a resolution of approximately 79 km on 60 vertical layers from the ground surface to a 0.1 hPa atmosphere using a 30-min time step (Berrisford et al., 2011). Many recent studies have indicated that microphysical choices have an impact on the



sensitivity and uncertainty of the WRF DSD model through simulation of typical rainfall events (Brown et al., 2016; Kala et al., 2015; Morrison et al., 2015; Yang et al., 2019).

3 | METHODOLOGY

3.1 | DSD model

The natural variation of the DSD model is commonly approximated using a normalized three-parameter (N_w , D_m , μ) gamma model (Dai & Han, 2014; Ulbrich, 1983) as follows:

$$N(D) = N_w f(\mu) \left(\frac{D}{D_m} \right)^\mu \exp \left[-\frac{(4+\mu)D}{D_m} \right], \quad (1)$$

$$f(\mu) = \frac{6(4+\mu)^{\mu+4}}{4^4 \Gamma(\mu+4)}, \quad (2)$$

where Γ denotes the mathematical gamma function, μ is the shape factor of the gamma DSD, N_w ($\text{mm}^{-1} \text{m}^{-3}$) is the normalized intercept parameter and D_m (mm) represents the volume-weighted diameter, which is defined as follows:

$$D_m = \frac{\int D^4 N(D) dD}{\int D^3 N(D) dD}. \quad (3)$$

Microphysics parameterization schemes can predict changes in moisture and precipitation fields in atmospheric models. They can be divided into bin and bulk schemes. In the bin approach, the size distribution of each hydrometeor is comprehensively computed; however, this requires storing variables for each bin with high cost for most mesoscale modelling applications (Cohard & Pinty, 2000). In simple bulk parameterization models, a functional form for the size distribution of each hydrometeor is assumed, and only the integral parameters of this distribution are computed during the model simulation to substantially reduce computational costs (Khain et al., 2000; Lim & Hong, 2010; Morrison et al., 2009). Most schemes use a constrained-gamma distribution model defined as follows:

$$N(D) = N_0 D^\mu \exp(-\lambda D), \quad (4)$$

where N_0 is the intercept and λ is the slope parameter of the size distribution, which can be extracted from the predicted mixing ratio q and number concentration N_c as follows:

$$\lambda = \left[\frac{c N_c \Gamma(\mu + d + 1)}{q \Gamma(\mu + 1)} \right]^{\frac{1}{d}}, \quad (5)$$

$$N_0 = \frac{N_c \lambda^{\mu+1}}{\Gamma(\mu+1)}, \quad (6)$$

where c and d are the coefficients of the assumed power law between mass and diameter ($m = cD^d$) that have been determined by the shape of precipitation particle. The shape parameter μ is usually set to 0 or 1 in most double-moment schemes (Johnson et al., 2016).

The space-borne DPR consists of Ku-band (13.6 GHz) and Ka-band (35.5 GHz) channels. This feature provides the opportunity to better detect raindrop characteristics, and the form of the DSD model is assumed to use a gamma distribution function (Equation 1). In the GPM DPR algorithm, μ is assumed to be 3 and the two types of R - D_m relationship are applied to stratiform precipitation in Equation (7) and convective precipitation in Equation (8); this is regarded as a primary assumption:

$$R = 0.401 \varepsilon^{4.649} D_m^{6.131}, \quad (7)$$

$$R = 1.370 \varepsilon^{4.258} D_m^{5.420}, \quad (8)$$

where ε is an adjustment factor and is constant in the retrieval process from the storm's top to the actual surface. Once ε is determined, R and D_m for each range bin can be searched in the scattering tables with given effective radar reflectivity factor (Z) values in the Ku-band, and then the path integrated attenuation (PIA) can be retrieved. By changing ε from 0.2 to 5.0, its most optimum value can be selected when the difference between the retrieved PIA and estimated PIA as per the surface reference technique is minimal. If Ka-band Z is available, the difference between the ε -retrieved Ka-band Z and the measured Ka-band Z is also used to adjust ε and can be applied to improve retrieval results (Chase et al., 2020; Leinonen et al., 2018). Note that in the surface clutter region, the Ku-band Z value is assumed to be the same as the clutter-free bottom value because it is not available for retrieval. After R and D_m are determined, N_w can be solved, as described in Section 3.2.

3.2 | Estimation of R , KE and Z using DSD

DSD parameterization models have been widely used in many environmental fields where rain rate and rainfall kinetic energy are the two core elements (e.g. precipitation microphysical processes, weather radar calibration and

soil erosion estimation). The $KE-R$ and $Z-R$ relationships are essential for a wide range of technologies. Rain rate R is dependent on the rainfall DSD, which is expressed as follows:

$$R = 6\pi \times 10^{-4} \int N(D)D^3V(D)dD, \quad (9)$$

where $V(D)$ is the raindrop fall velocity that can be estimated from a power law empirical relationship with raindrop diameter (Atlas & Ulbrich, 1977) by using the following equation considered suitable for Chilbolton, United Kingdom (Islam et al., 2012):

$$V_i(D) = 3.78D_i^{0.67}. \quad (10)$$

$KE-R$ dominates the ability of a raindrop to detach soil particles. Rainfall KE and R are functions of the local climate and precipitation microphysics at the measured location; these parameters allow for the estimation of rainfall erosivity. The kinetic energy e (J) of a raindrop with mass m (g) and terminal velocity v (m s^{-1}) is defined as follows:

$$e = \frac{1}{2}mv^2. \quad (11)$$

Assuming a spherical volume for every raindrop shape, the mass of a drop can be calculated using the cube of diameter D (mm). Considering the instrument (e.g. disdrometer) sample drop size, the mean radius and falling velocity of the corresponding sampling drop size class used to represent D and v are expressed as D_i and v_i , respectively. In such cases, e_i of any drop pertaining to a given class is given as follows:

$$e_i = \frac{1}{12} \times 10^{-9} \rho v_i^2 D_i^3, \quad (12)$$

where ρ is the density of water (g cm^{-3}). The sum of the kinetic energy of each raindrop, within a given rain depth that hits a given area, defines the total kinetic energy. The unit rainfall kinetic energy KE_v , for the unit rainfall depth ($\text{J m}^{-2} \text{mm}^{-1}$) and KE_t for the unit time ($\text{J m}^{-2} \text{h}^{-1}$) can be calculated as the product of the kinetic energy of each drop of each diameter class, which can be expressed as follows:

$$KE_v = \frac{e_{sum}}{V_t A P_t} = \frac{1}{V_t A P_t} \sum_{i=1}^{ni} N_i e_i, \quad (13)$$

$$KE_t = \frac{e_{sum}}{60 A P_t} = \frac{1}{60 A P_t} \sum_{i=1}^{ni} N_i e_i, \quad (14)$$

where A represents the sample area of the sensor, P_t is the rainfall depth at the t -th minute, N_i is the number of drops in class i and V_t indicates the rainfall depth during time t . All the instruments can sum up the number of raindrops in each sampling class and produce the raindrop spectra for a time step. Then, we can obtain KE and R for each time step to find the relationship between them.

Another important relationship, the $Z-R$ relationship is mostly expressed in power law terms, such as $Z = aR^b$. This relationship plays an important role in improving radar QPE. In computing the radar reflectivity factor (Z), Rayleigh scattering has been assumed; accordingly, Z can be written as follows:

$$Z = \int N(D)D^6 dD. \quad (15)$$

This equation can be related to the DSD and expressed in units of $\text{mm}^6 \text{m}^{-3}$.

3.3 | Evaluation methods

To quantitatively reveal the increasing trend of the DSD parameters with rain rate, the R values were divided into six scenarios, $0.1 \leq R < 0.5$, $0.5 \leq R < 1$, $1 \leq R < 2$, $2 \leq R < 4$, $4 \leq R < 8$ and $R > 8 \text{ mm h}^{-1}$, labelled as R1...R6, respectively. The raindrop microphysics between GPM DPR measurements and WRF simulation were also investigated, and subsequently validated using a disdrometer. Several indicators were used to evaluate the WRF- and DPR-derived DSD performance (i.e. accuracy of rainfall estimation), including Pearson's correlation coefficient, mean absolute error (MAE) and root mean squared error ($RMSE$). Pearson's correlation coefficient is a measure of the linear correlation between two variables and is defined as follows:

$$\text{Pearson} = \frac{n \sum R_{D_i} \sum R_{W_i} - \sum R_{D_i} \sum R_{W_i}}{\sqrt{n \sum R_{D_i}^2 - (\sum R_{D_i})^2} \sqrt{n \sum R_{W_i}^2 - (\sum R_{W_i})^2}}, \quad (16)$$

where n is the number of time steps. Considering that this correlation cannot reveal the absolute bias of measured values, the MAE and $RMSE$ are used and defined as follows:

$$MAE = \frac{\sum |R_{W_i} - R_{D_i}|}{n}, \quad (17)$$

$$RMSE = \sqrt{\frac{1}{m} \sum [h(x_i) - y_i]^2}. \quad (18)$$

The two indicators are frequently used to measure the differences between the simulated or predicted values and the observed values, with the perfect score being 0. RMSE is the square root of the average of squared errors, which is used to measure the deviation between the observation value and the true value; MAE is the average value of absolute errors, which can better describe the predicted value error in time series analysis.

4 | RESULTS

4.1 | DSD parameter estimation by WRF model and GPM

In this study, we used WRF model version 3.8, which down-scaled the ERA-Interim data for every 15 min. A $2 \times 2 \text{ km}^2$ grid domain unit centred at the Chilbolton Observatory was chosen as WRF sample area, and used the Thompson aerosol-aware scheme (Thompson & Eidhammer, 2014). The Thompson aerosol-aware scheme can predict the ice nuclei and cloud condensation nuclei number concentrations using the fixed- μ gamma distribution with $\mu = 0$ (Thompson & Eidhammer, 2014). This parameterization scheme demonstrates excellent performance in the WRF model when simulating the DSD for Chilbolton (Yang et al., 2019). Other physical parameterizations include the Kain–Fritsch cumulus scheme (Kain, 2004), the Mellor–Yamada–Janjić planetary boundary layer scheme (Janjić, 1994), the RRTM longwave radiation scheme (Mlawer et al., 1997), the Dudhia shortwave radiation scheme (Dudhia, 1989) and the Noah land-surface model (Ek et al., 2003). The domain setting was the same as that adopted by Yang et al. (2019); that is, 18, 6 and 2 km for the outer, middle and inner nested domains, respectively.

In GPM DPR files, the variable named paramDSD is generated by the DPR Solver module to save the parameters of DSD functions, including D_m and N_w of each scan pixel. The long revisit times of the GPM core satellite imply that precipitation observations in any region are discontinuous. Considering the disdrometer DSD is point-based, GPM data are selected in a rectangular domain of size 1° (longitude) \times 1° (latitude), which is centred at the location of the Chilbolton disdrometer to ensure sufficient number of GPM samples and to avoid the interference from the ocean and complex topography (Radhakrishna et al., 2016). To obtain more sampling points, we used the DPR data between May 2014 and December 2019 for comparison; this period was observed after the satellite had stabilized at the nominal observation altitude (Hamada & Takayabu, 2016).

To reduce the measurement error of small raindrops, we selected data with a rain rate of $>0.1 \text{ mm h}^{-1}$ for

comparison (Angulo-Martínez et al., 2016). GPM samples with $R < 0.2 \text{ mm h}^{-1}$ were discarded owing to radar sensitivity limitations. The values of N_w in the DSD spectra derived by the disdrometer for over 4 years reached $10^5 \text{ mm}^{-1} \text{ m}^{-3}$, with the lowest values being $<10 \text{ mm}^{-1} \text{ m}^{-3}$. Therefore, we calculated the log of N_w ($\log_{10}N_w$) for intuitive comparison. Figure 2 shows the D_m and $\log_{10}N_w$ maps obtained using the WRF model at the time of rain (January 3, 2015 12:00:00). The two maps are centred on the disdrometer location, covering an area of $90 \times 90 \text{ km}^2$. The D_m and $\log_{10}N_w$ sometimes show positive and sometimes negative correlation, indicating the spatial complexity of the rainfall process and the necessity for studying spatial DSD on a large scale.

For our experiment, we used a $2 \times 2 \text{ km}^2$ WRF grid covering the Chilbolton Observatory. As the number of sample points in the three datasets are different (112,067 for the disdrometer, 4093 for the WRF model and 10,503 for GPM), we compared the cumulative density distributions of the DSD parameters retrieved by each method (Figure 3). The curves of the WRF model and the disdrometer show the greatest similarity, although the WRF model had larger D_m and smaller N_w compared with that of the disdrometer. This difference may be caused by the absence of convective precipitation in the WRF model, which is explained in detail in Section 4.2. At extremely low and high parameter values, variation is evident between the disdrometer and the GPM. Because of limitations in the sensitivity of the DPR, only rain rates greater than 0.5 mm h^{-1} are processed (Iguchi et al., 2018; Radhakrishna et al., 2016). This feature affects the DSD parameters that are associated with the rain intensity observed by DPR. Thus, the cumulative distribution function (CDF) curves of GPM D_m and $\log_{10}N_w$ display the characteristics of small value ranges and large intermediate slopes. Moreover, the numbers of all three types of data were sufficient for the statistical analysis.

4.2 | Relationships between DSD parameters and rain rate

DSD varies depending on the rain type; the distribution of $\log_{10}N_w$ – D_m is an indicator used to separate convective and stratiform rain types (Ji et al., 2019). Here, we separated disdrometer raindrops into two groups – convective and stratiform – using the standard deviation method described by Bringi et al. (2003). Figures 4 and 5 compare the relationships of D_m – R and $\log_{10}N_w$ – D_m derived from the disdrometer, WRF model and GPM DPR estimations. The blue and green dots represent the convective and stratiform samples observed by the disdrometer, respectively. The separation line between the two groups of

FIGURE 2 Maps of WRF-derived D_m (a) and $\log_{10}N_w$ (b) (January 3, 2015 12:00:00), centred on Chilbolton Observatory (marked as \times). WRF, weather research and forecasting

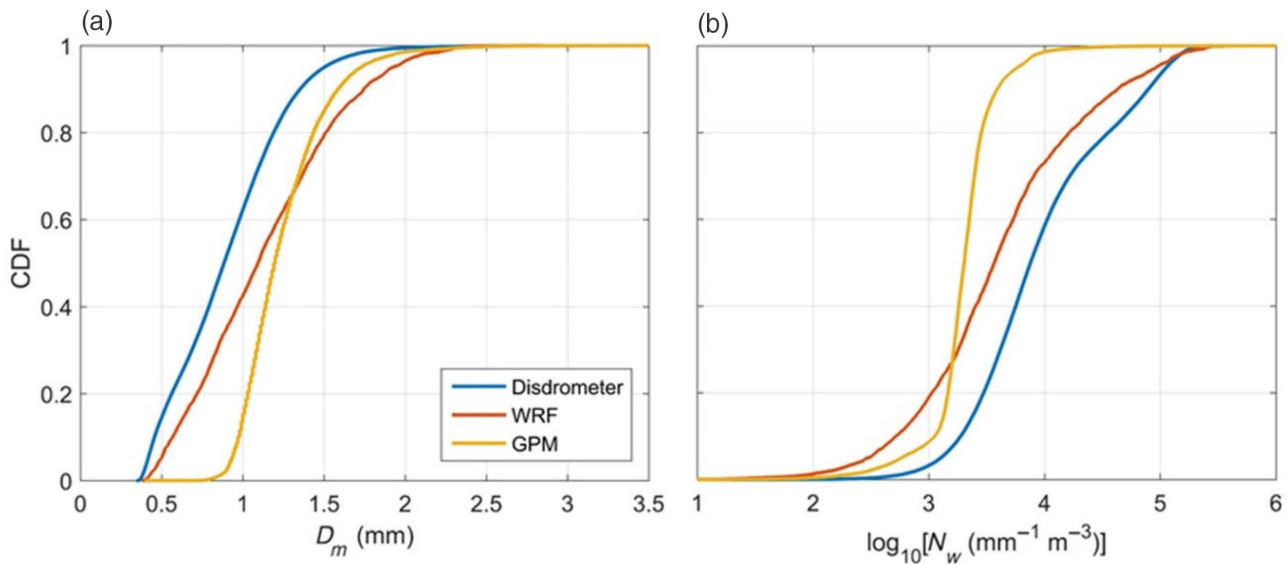
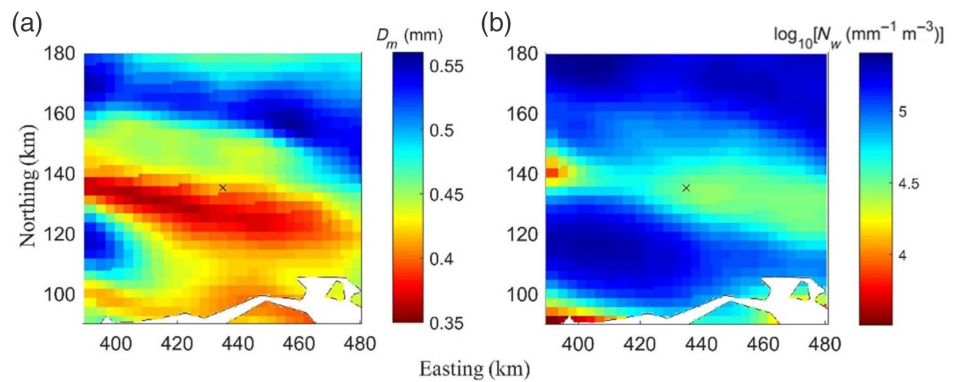


FIGURE 3 CDF of D_m (a) and $\log_{10}N_w$ (b) from disdrometer, WRF and GPM DPR. CDF, cumulative distribution function; DPR, dual-frequency precipitation radar; GPM, global precipitation measurement mission; WRF, weather research and forecasting

data was regarded as the standard for the division of local rainfall types. The results show that the WRF model and GPM DPR samples are mainly concentrated in the stratiform group of the disdrometer drops. In fact, the cumulus scheme is not used in the WRF model physics parameterizations, where convective rainfall generation is assumed to be entirely resolved (Yang et al., 2019). Therefore, the WRF model outputs do not involve convective rain with high D_m and N_w values (green dots in Figure 5). The GPM not only measured a large amount of stratiform rain, but also observed a small amount of convective precipitation and samples with high N_w and high R throughout the study area. In Figure 4, the D_m values from all measurements seldom exceed 2 mm and show an approximate exponential increasing trend with respect to rain rate. Under the same R value, the mean raindrop diameter of GPM samples is the largest, followed by that of the WRF model. DSDs derived from the WRF model rely heavily on microphysical schemes, while GPM-

derived DSD results are affected by limitations in radar sensitivities. Therefore, in comparison, the disdrometer results show that DSDs exhibit higher variability. Figure 5 shows the scatterplot of $\log_{10}N_w$ versus D_m for different DSD instruments. The domain shows a very clear separation between stratiform and convective precipitation in disdrometer data points. All three types of $\log_{10}N_w$ - D_m samples almost completely coincide in the stratiform raindrop spectra. For smaller diameters, the WRF results show raindrops with a lower concentration variation than those observed using the disdrometer; GPM events have the highest concentrations.

Figure 6 specifically compares the $\log_{10}N_w$ - D_m frequencies from different measurements. Here, the number of occurrences refers to the total number of 0.05 units of D_m and $\log_{10}N_w$. The $\log_{10}N_w$ - D_m domain of the disdrometer is obviously concentrated in the entire range of GPM measurement results; the highest number of occurrence is in the ranges of $D_m = \sim 0.3$ - 0.4 and

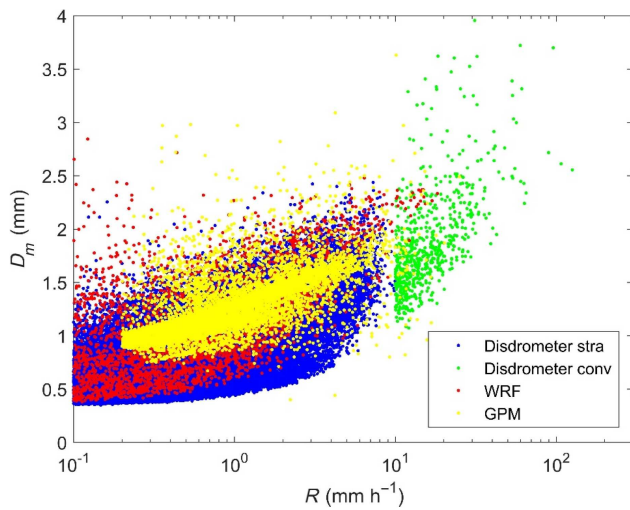


FIGURE 4 Scatter diagrams of relationship between D_m and R from disdrometer, WRF model and GPM DPR. conv, convective precipitation; DPR, dual-frequency precipitation radar; GPM, global precipitation measurement mission; stra, stratiform precipitation; WRF, weather research and forecasting

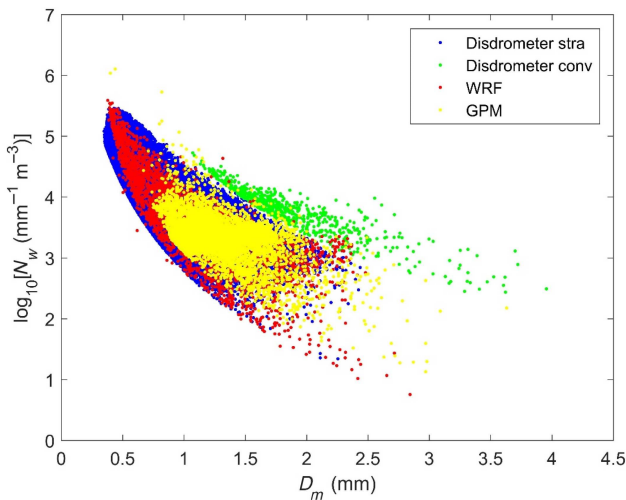


FIGURE 5 Scatter diagrams of relationship between $\log_{10}N_w$ and D_m from disdrometer, WRF model and GPM DPR. conv, convective precipitation; DPR, dual-frequency precipitation radar; GPM, global precipitation measurement mission; stra, stratiform precipitation; WRF, weather research and forecasting

0.8–1.1 mm, with the corresponding $\log_{10}N_w$ being in the ranges of ~ 4.6 – 5.2 and 3.7 – 4.0 units, respectively. Compared with that of the disdrometer, the $\log_{10}N_w$ – D_m domain of the WRF model has lower concentrations throughout the entire D_m range; however, the density is similar between $0.5 < D_m < 1.5$ mm, and reaches a maximum at $D_m = 1.4$ mm. To ensure that the WRF microphysical scheme matches the spatial and temporal changes and particularities of regional precipitation, merging the surface observation data is necessary to

modify the WRF DSD parameters; this should be implemented in a future work.

Figure 7 shows the average values of D_m and $\log_{10}N_w$ versus the six R sets obtained from the disdrometer (blue lines), WRF model (red lines) and GPM (yellow lines). The mean D_m value increases with the growth of the rain rate, while the mean $\log_{10}N_w$ seems to have no obvious change, even though all three lines change monotonically (Figure 7b). Under the same R class, the mean D_m measured by the disdrometer is always the lowest among the three data points, whereas the N_w values are the highest. Apparently, the high concentrations of the disdrometer raindrop spectrum are caused by convective rain with high N_w values. Both the average D_m and $\log_{10}N_w$ of the GPM are the same as the WRF results under the R4 class. Moreover, the differences between the disdrometer and GPM lines gradually decrease as the rain rates increase, and become very low at R6. The large differences under low rain rates reflect the sensitivity limitation of DPR measurements.

4.3 | KE – R relationship estimation and error analysis

The total kinetic energy estimation of a rainfall event is usually estimated by summing up the individual kinetic energies of raindrops, based on its relationship with rainfall intensity (R) (Brown & Foster, 1987; Davison et al., 2005; Wischmeier & Smith, 1978). The performances of the unit kinetic energy–rain rate relationship estimated using Equations (13) and (14) are compared in Figure 8. The black lines indicate the fitted relationship using disdrometer observations with $R^2 (KE_v-R) = 0.44$ and $R^2 (KE_t-R) = 0.92$. R^2 is the proportion of the variance in the dependent variable, which can be predicted using the independent variable. It provides a measure of how well-observed outcomes are replicated by the model based on the proportion of the total variation of outcomes explained by the model.

The KE (including KE_v and KE_t)– R scatters of WRF simulations are closer to the disdrometer trend lines than those of the GPM KE – R results with lower rain rates ($R < 2$ mm h^{-1}). In contrast, the KE values from WRF model tended to be overestimated (most data points are above the black line) with increasing R . In terms of the KE_v – R relationship, exponential functions, formed as $KE_v = a[1-b * \exp(-cR)]$ have been widely used (Lim et al., 2015; Petan et al., 2010; Renard, 1997; Van Dijk et al., 2002), especially in soil erosion models including the Revised Universal Soil Loss Equation (Renard, 1997). Here, the KE_v values tended to be stationary when the rain rate reached approximately 10 mm h^{-1} ; however, the

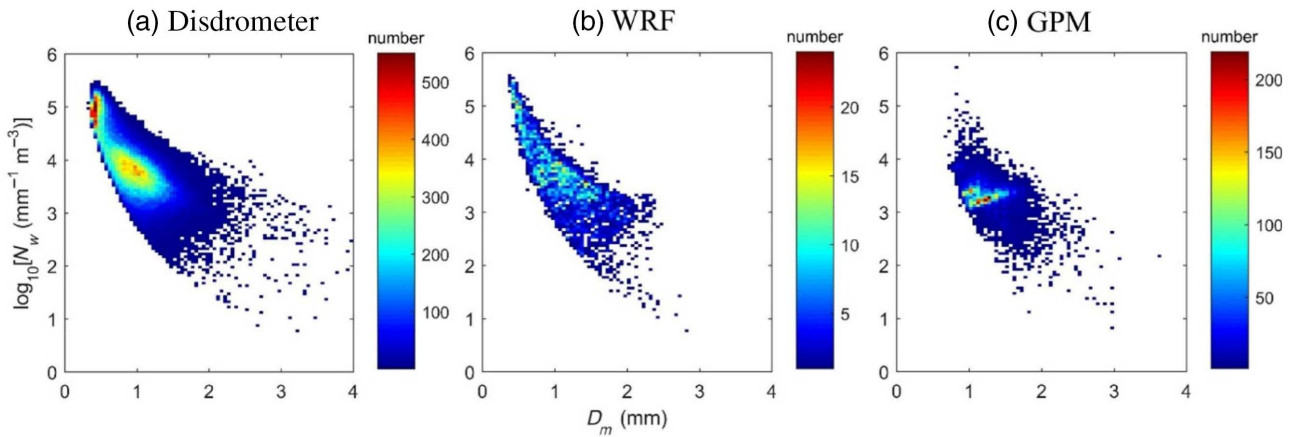


FIGURE 6 Occurrences of relationship between $\log_{10}N_w$ and D_m from disdrometer (a), WRF model (b) and GPM DPR (c) per unit D_m and $\log_{10}N_w$. DPR, dual-frequency precipitation radar; GPM, global precipitation measurement mission; WRF, weather research and forecasting

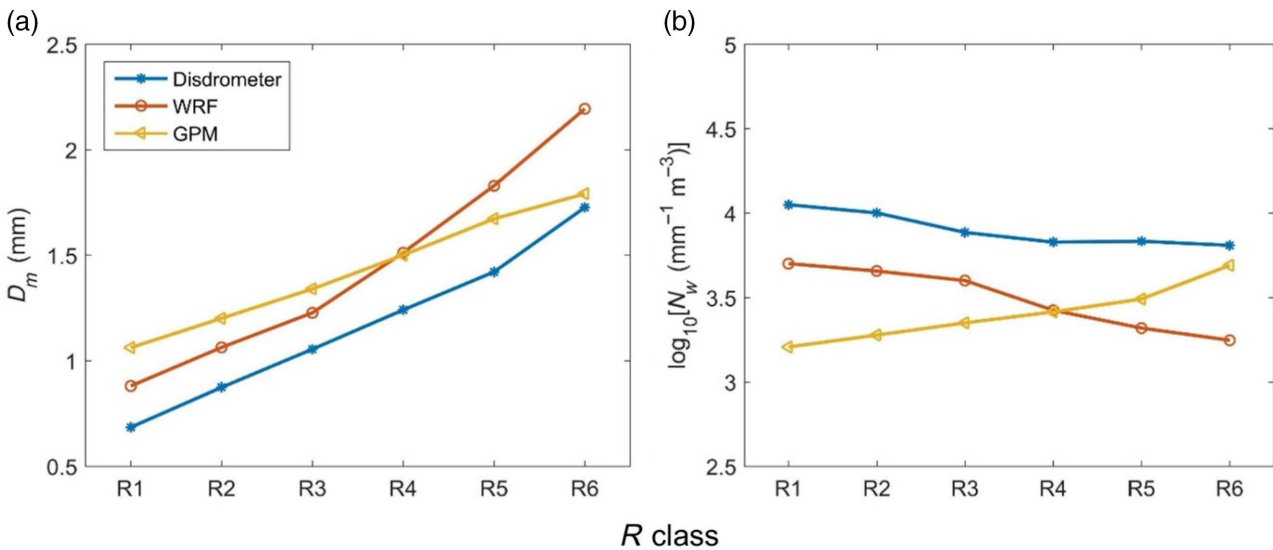


FIGURE 7 Comparison of mean D_m - R (a) and mean $\log_{10}N_w$ - R (b) in the six R classes from disdrometer, WRF model and GPM DPR. DPR, dual-frequency precipitation radar; GPM, global precipitation measurement mission; WRF, weather research and forecasting

maximum value was roughly equal to $16.08 \text{ J m}^{-2} \text{ mm}^{-1}$, which is the same as the coefficient of the KE_v - R exponential trend line formula obtained from the disdrometer data. The relationship between KE_t and R is evident (Figure 8), and can be described by a power law function (formed as $KE_t = aR^b$; Meshesha et al., 2016). The values of KE_t estimated by GPM were the highest, with most of the sample points being higher than the trend line. The high R^2 of WRF KE_v - R (0.97) also shows the strong fitting relationship for WRF retrievals. We observed a deviation in the slope between the results of the WRF model and the disdrometer, which may be related to the overestimation of D_m derived by WRF model during high rainfall. The dispersion evaluation indicators (MAE , $RMSE$ and Pearson) of the KE - R samples versus disdrometer-based formulas are listed in Table 1. The GPM scheme performed better

(i.e. lower MAE and $RMSE$ and the same Pearson) compared with WRF simulations in the KE_v - R domain. The WRF model has a better Pearson value for KE_t - R compared with the DPR observations. The primary difference between GPM DPR and WRF model in DSD retrieval is that the processes are achieved through measurement and simulation, respectively. The DPR derives rainfall micro-physical characteristics by observing radar signals that come in direct contact with raindrops, while the WRF model uses mesoscale meteorological data to simulate rainfall processes through a series of numerical simulations. Although both DPR and WRF model rely on important assumptions, there are still differences in the directness of rainfall characteristics estimation.

In Figure 9, KE_t and KE_v show an increasing trend with respect to rain rate. The polyline values of GPM and

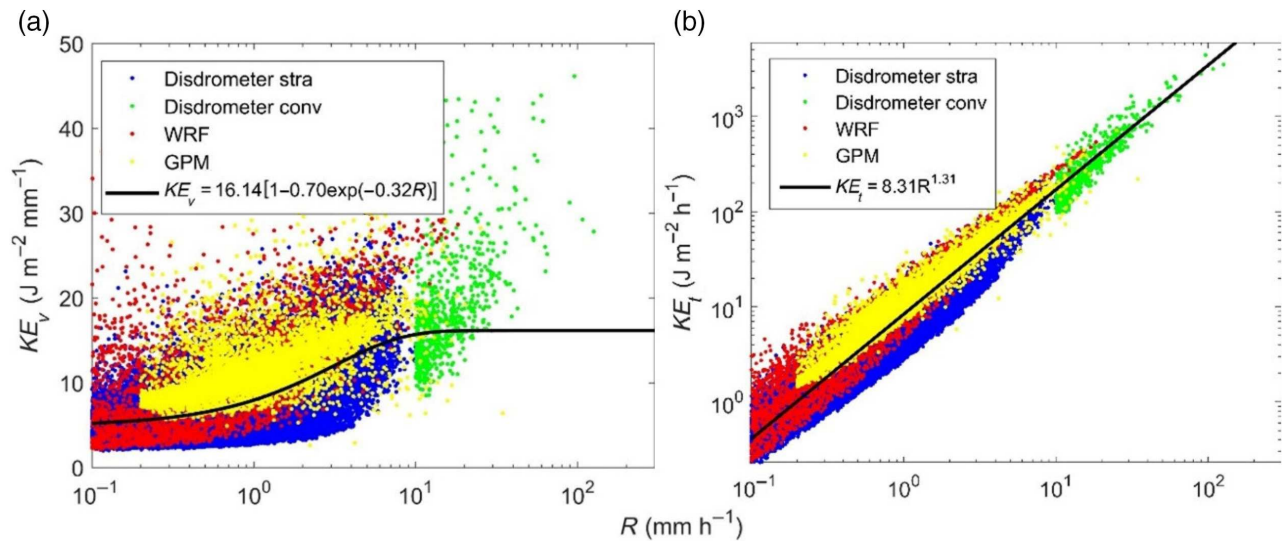


FIGURE 8 Scatter diagram of KE_v - R (a) and KE_t - R (b) from disdrometer, WRF model and GPM DPR and the fitted relationships based on the disdrometer. conv, convective precipitation; DPR, dual-frequency precipitation radar; GPM, global precipitation measurement mission; stra, stratiform precipitation; WRF, weather research and forecasting

TABLE 1 Evaluated indicator comparison of WRF- and GPM-derived KE_v - R and KE_t - R , taking the fitted relationships as standards

	KE_v			KE_t		
	MAE	RMSE	Pearson	MAE	RMSE	Pearson
WRF model	4.10	5.59	0.66	7.38	16.83	0.98
GPM	3.38	4.09	0.66	5.11	12.44	0.91

Abbreviations: GPM, global precipitation measurement mission; MAE, mean absolute error; RMSE, root mean squared error; WRF, weather research and forecasting.

WRF model are extremely similar under R1 to R4 and are always higher than the disdrometer values. The results also show that WRF KE s have been overestimated; in particular, the differences between mean WRF KE_v and mean disdrometer KE_v increased as the R class increased. The WRF KE s were consistently the highest except at low rain rates ($R < 2 \text{ mm h}^{-1}$). Based on our results and the physical assumptions of the scheme, we suggest that WRF DSD may be suitable for simulating parameters that have a strong relationship with rain rate. At the same time, mean GPM KE values are close to the disdrometer measurements, which may also be due to fewer data points with high rain rates that were measured by the DPR.

4.4 | Z-R relationship estimation and error analysis

The key problem of Z - R relationships is their limited spatial and temporal representativeness because DSD exhibits an appreciable amount of spatial and temporal variability (Chapon et al., 2008; Uijlenhoet et al., 2003).

Power law terms, such as $Z = aR^b$, are widely used to describe the relationship between radar reflectivity and rain rate. Note that the radar reflectivity factor, Z , is calculated from Equation (15), which assumes Rayleigh scattering and is independent of frequency. As shown in Figure 10, a power-based smooth line relating Z and R was generated to fit the disdrometer data, with values of R^2 reaching 0.80. The fitted Z - R relationship of the disdrometer is slightly different from the standard Z - R equation for the entire UK radar rainfall estimation ($Z = 200R^{1.6}$). The WRF model and GPM provide the opportunity to deduce the Z - R relationship of any given area and can better reflect dynamic changes in the Z - R relationship caused by changes in DSD.

Figure 11 summarizes the mean Z values for each R class. The overall trends of the three are similar. The mean Z value of the disdrometer is almost consistently the lowest, and its logarithmic change curve is approximately parallel to that of the WRF model. This condition indicates that the Z difference between the WRF simulations and disdrometer increases by a power of $10 \text{ mm}^6 \text{ m}^{-3}$ with increasing rain rate, thereby predicting huge WRF deviation

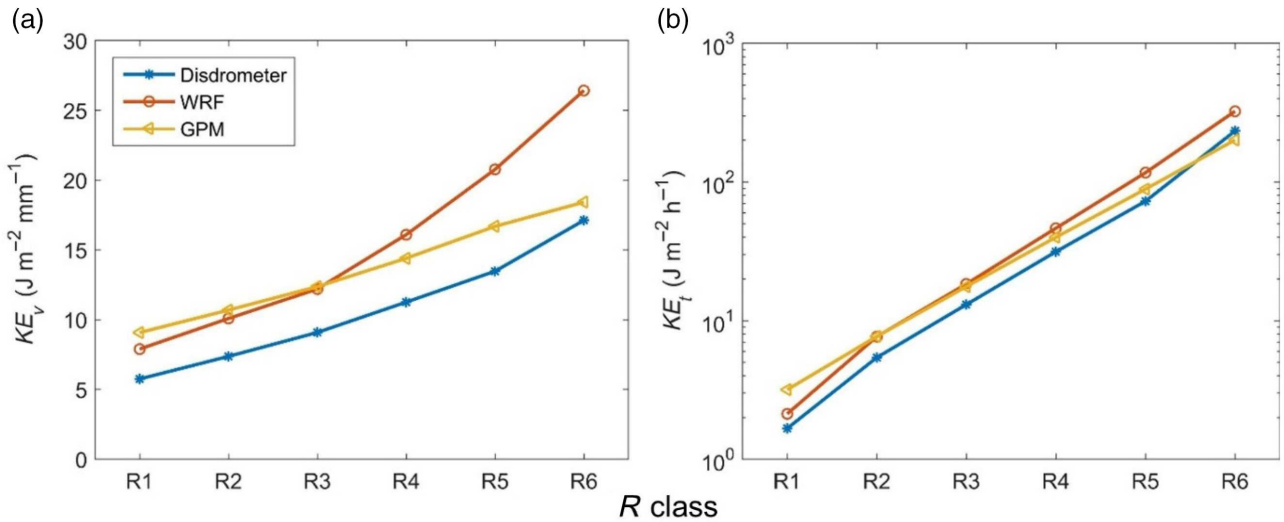


FIGURE 9 Comparison of relationship between KE_v and R (a) and relationship between KE_t and R (b) in the six R classes from disdrometer, WRF model and GPM DPR. DPR, dual-frequency precipitation radar; GPM, global precipitation measurement mission; WRF, weather research and forecasting

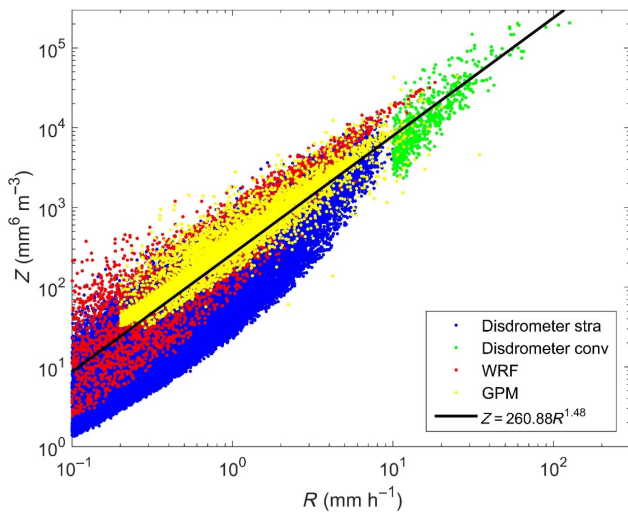


FIGURE 10 Scatter diagram of relationship between Z and R from disdrometer, WRF model and GPM DPR and the fitted power-law relationship based on the disdrometer. conv, convective precipitation; DPR, dual-frequency precipitation radar; GPM, global precipitation measurement mission; stra, stratiform precipitation; WRF, weather research and forecasting

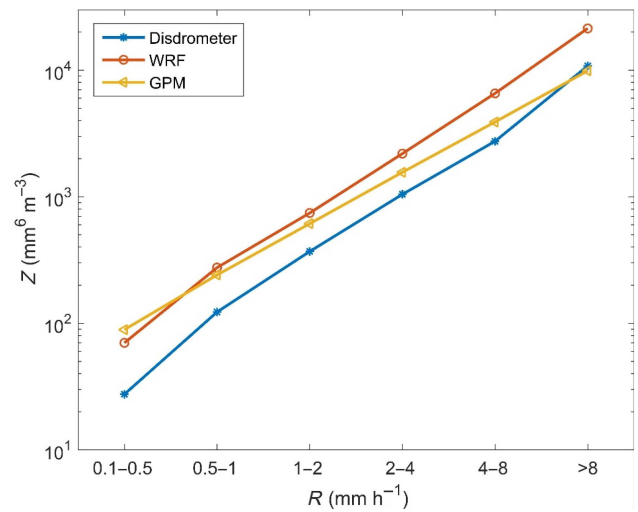


FIGURE 11 Mean Z of different R classes from disdrometer, WRF model and GPM DPR. DPR, dual-frequency precipitation radar; GPM, global precipitation measurement mission; WRF, weather research and forecasting

when simulating heavy rainfall. At the same time, although Z values of GPM are overestimated, they are close to the disdrometer results for rain rates greater than $0.5 mm h^{-1}$, which is also the minimum measurable rain rate that KuPR and KaPR can detect simultaneously.

Figure 12 shows the cumulative density functions of Z corresponding to the six rain rate classes. In most cases, the CDF curve of the disdrometer (blue lines) is located at the highest of the three, indicating that the Z values obtained by the disdrometer are consistently lower under

the same rain rate. In lower R classes (R1 to R3), Z of WRF simulations showed a faster growth in CDF than that of GPM, but the CDF was overtaken by GPM. Instead, the GPM curves become close to the disdrometer curves, especially under heavy rain (R6), at which point the two curves almost coincide. With the disdrometer CDF curve as a reference, the WRF and GPM results show high Z values in each diagram, especially the WRF simulations. Table 2 summarizes the two deviations of CDF of the WRF simulations and GPM versus the disdrometer results. With an increase in the rain rate, the errors of WRF CDF gradually increased. The Pearson coefficient

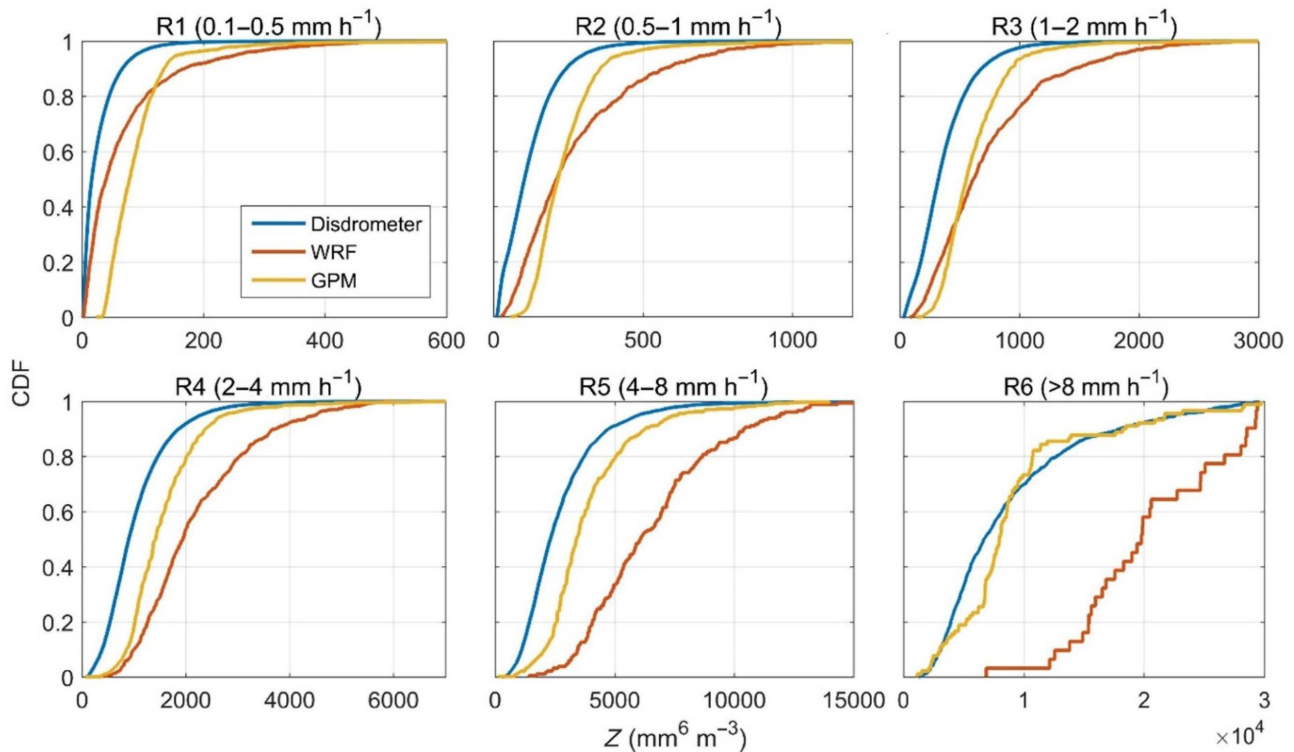


FIGURE 12 CDF of Z in the six R classes from disdrometer, WRF model and GPM DPR. DPR, dual-frequency precipitation radar; GPM, global precipitation measurement mission; WRF, weather research and forecasting

R class	WRF model			GPM		
	MAE	RMSE	Pearson	MAE	RMSE	Pearson
R1	0.00	0.02	0.94	0.00	0.03	0.90
R2	0.01	0.03	0.91	0.00	0.04	0.93
R3	0.01	0.06	0.92	0.01	0.05	0.95
R4	0.04	0.12	0.89	0.02	0.07	0.96
R5	0.13	0.24	0.82	0.04	0.09	0.97
R6	0.39	0.45	0.74	0.04	0.06	0.98

TABLE 2 Indicator comparison of CDF for WRF- and GPM-derived Z - R of the six R classes, taking the fitted relationships as standards"

Abbreviations: CDF, cumulative distribution function; GPM, global precipitation measurement mission; MAE, mean absolute error; RMSE, root mean squared error; WRF, weather research and forecasting.

continued to decrease, falling below 0.9 at the R4 class. However, starting from R1, the GPM Pearson was consistently above 0.9, reaching 0.98 in R6; the performances of MAE and RMSE were consistently better than those of WRF simulations. The results show that GPM and WRF errors are stable, and GPM performs better than WRF model despite the limited samples for low rain rates.

5 | DISCUSSION

Disdrometers are accurate devices used to obtain rainfall characteristics, but their high cost hinders their

application in large domains. This study shows that the WRF model and GPM can be used to obtain rainfall DSD and microphysical characteristics with acceptable errors; for example, Pearson values of KE_r - R of >0.90 were exhibited for both WRF model and GPM, indicating that the WRF model and GPM are good complementary tools for disdrometer applications. Although these two large-scale methods may not be able to accurately obtain DSD at certain times and locations, they are powerful tools for solving key issues with dynamic rainfall microphysics, such as KE - R and Z - R relationships. At present, the relationships between KE - R and Z - R are unchanged in most applications, which is unreasonable and does not

conform to the DSD reality of temporal and spatial changes. Therefore, obtaining dynamic DSD using only disdrometers is difficult; WRF simulations and GPM measurements offer supplementary methods.

The WRF model has a clear physical process and good potential for handling some rainfall features with 3D/4D non-hydrostatic methods. Its reliability is heavily dependent on the model driving the initial data provided by mesoscale or global models and complicated scheme setting and parameter adjustment (Kumar et al., 2017; Liu et al., 2013; Thompson & Eidhammer, 2014). However, many uncertainties are found in the parameterization of the WRF simulation, and the choice of microphysical schemes has a great influence on inverted DSD (Ćurić et al., 2009; Yang et al., 2019). The rainfall DSD can also be influenced by the quality of the meteorological dataset. In future work, we plan to compare or integrate several sources of meteorological data to decrease to the greatest extent possible the uncertainty induced in WRF modelling. GPM measurements have high spatial resolution owing to the radar echoes transmitted by DF radar on the core satellite. However, it may not be possible to obtain global raindrop characteristics at the same time or to capture a full storm because of the long revisit time of the satellite, resulting in poor time resolution. Therefore, GPM-derived DSD can be used to investigate rainfall characteristics that do not require continuous data and summarize the DSD microphysical changes (such as the $KE-R$ and $Z-R$ relationships analysed in this work) at different times and for different places. WRF model can simulate continuous long-term DSD and analyse the detailed rainfall characteristics of storms. Compared with the observation methods, the results simulated by WRF model were more aggregated and regular. In accordance with the results, WRF provides more accurate DSD estimation under low rain rates. At high rain rates, GPM-derived DSD may be more reliable for use with acceptable error.

Fusing the DSDs obtained by the disdrometers, WRF model and GPM is valuable, and we recommend the development of a data fusion algorithm to harness the advantages of multiple data sources. The GPM mission deployed several temporary disdrometers, including JWD and 2D-video disdrometers (2DVDs), around the world for experimental validation. Thus, after disdrometer calibration, global observations from GPM could be used to modify the WRF model to ensure that its physical process is more reasonable; this offers a promising method for large-scale high-precision DSD estimation. Accurately measured GPM information with low time resolution can determine the selection of WRF physical processes and model correction. We can analyse GPM measurements to retrieve the raindrop

characteristics of sites or regions with similar geographical features based on a large number of long-interval scan results, and subsequently use them to adjust the simulation settings or correct deviations of the WRF model for obtaining high-accuracy rainfall microphysics estimation on a large scale. To achieve data fusion precisely, we must recognize the uncertainties of each method; this will be the focus of a future work.

6 | CONCLUSION

Rainfall microphysical processes play an important role in many disciplines, such as hydrology and meteorology. However, estimation traditionally relies on disdrometers, which are not widely distributed owing to the massive cost. To explore other methods for large-scale inversion of rainfall microphysics, we extracted rainfall characteristics, including drop size distribution (DSD) parameters, rain rate, kinetic energy and radar reflectivity, retrieved from the weather research and forecasting (WRF) estimation and global precipitation measurement mission (GPM) measurements over 4 years (GPM data were retrieved for over 6 years approximately) and compared them with disdrometer observations.

Few of the mass-weighted mean drop diameter values for Chilbolton (United Kingdom), which were derived from each DSD source, exceed 2 mm. The $\log_{10}N_w-D_m$ domain for the disdrometer was evidently concentrated within the range of the GPM measurement results, and its density reached the peak at $D_m = 1$ mm. The DSD parameter distribution trends of the three approaches were similar, although convective rainfall was ignored by the WRF model, and the GPM dual-frequency precipitation radar (DPR) captured little convective precipitation. Although the WRF DSD approach underestimated the rain rate to some extent, it is suitable for simulating parameters that have a strong relationship with rain rate, such as the $KE-R$ and $Z-R$ relationships. Finally, under the same rain rate, the WRF model and GPM slightly overestimated KE and Z . WRF simulations was accurate in light rain ($R < 0.5 \text{ mm h}^{-1}$), while GPM was the most accurate when the two DPR radars could be fully used ($R > 0.5 \text{ mm h}^{-1}$).

In this study, we overcame the limitations of DSD obtained by traditional instruments and comparatively evaluated the performances of WRF model and GPM for estimating DSD. GPM DSDs were derived from DPR measurements and corrected using ground-based disdrometers. GPM can deduce accurate rainfall microphysical relationships. Meanwhile, WRF underestimates the rain rate, resulting in poor estimation. However, GPM could be used as a WRF correction because of its continuous data and rare high R observations. We used the

rainfall data from Chilbolton for the DSD comparisons, and our conclusions may not necessarily represent other situations completely. In future studies, we will analyse the large-scale uncertainties of all three methods and compare them at typical settings to obtain reliable conclusions.

ACKNOWLEDGEMENTS

This study was supported by the National Natural Science Foundation of China (Nos. 41871299, 41771424 and 42071364), and the National Key R&D Program of China (Nos. 2018YFB0505500 and 2018YFB0505502).

DATA AVAILABILITY STATEMENT

The disdrometer data at Chilbolton was sourced from the Met Office Integrated Data Archive System (MIDAS) available from the NCAS British Atmospheric Data Centre (<http://archive.ceda.ac.uk/>). The 2ADPR NS data can be obtained at the NASA GPM website (<https://pmm.nasa.gov/data-access/downloads/gpm>). The ERA-Interim data driving the WRF model can be downloaded from the ECMWF Public Datasets web interface (<https://www.ecmwf.int/>).

ORCID

Qiang Dai  <https://orcid.org/0000-0002-8359-5892>

REFERENCES

- Angulo-Martinez, M., Begueria, S., Navas, A. & Machin, J. (2012) Splash erosion under natural rainfall on three soil types in NE Spain. *Geomorphology*, 175, 38–44.
- Angulo-Martinez, M., Begueria, S. & Kysely, J. (2016) Use of disdrometer data to evaluate the relationship of rainfall kinetic energy and intensity (KE-I). *Science of the Total Environment*, 568, 83–94.
- Atlas, D. & Ulbrich, C.W. (1977) Path-and area-integrated rainfall measurement by microwave attenuation in the 1–3 cm band. *Journal of Applied Meteorology*, 16(12), 1322–1331.
- Berrisford, P., Källberg, P., Kobayashi, S., Dee, D., Uppala, S., Simmons, A. et al. (2011) Atmospheric conservation properties in ERA-Interim. *Quarterly Journal of the Royal Meteorological Society*, 137(659), 1381–1399.
- Brandes, E.A., Zhang, G. & Vivekanandan, J. (2004) Drop size distribution retrieval with polarimetric radar: model and application. *Journal of Applied Meteorology*, 43(3), 461–475.
- Bringi, V., Chandrasekar, V., Hubbert, J., Gorgucci, E., Randeu, W. & Schoenhuber, M. (2003) Raindrop size distribution in different climatic regimes from disdrometer and dual-polarized radar analysis. *Journal of the Atmospheric Sciences*, 60(2), 354–365.
- Brown, L. & Foster, G. (1987) Storm erosivity using idealized intensity distributions. *Transactions of the ASAE*, 30(2), 379–386.
- Brown, B.R., Bell, M.M. & Frambach, A.J. (2016) Validation of simulated hurricane drop size distributions using polarimetric radar. *Geophysical Research Letters*, 43(2), 910–917.
- Chapon, B., Delrieu, G., Gosset, M. & Boudevillain, B. (2008) Variability of rain drop size distribution and its effect on the Z–R relationship: a case study for intense Mediterranean rainfall. *Atmospheric Research*, 87(1), 52–65.
- Chase, R.J., Nesbitt, S.W. & McFarquhar, G.M. (2020) Evaluation of the microphysical assumptions within GPM-DPR using ground-based observations of rain and snow. *Atmosphere*, 11(6), 619.
- Cohard, J.M. & Pinty, J.P. (2000) A comprehensive two-moment warm microphysical bulk scheme. I: description and tests. *Quarterly Journal of the Royal Meteorological Society*, 126(566), 1815–1842.
- Ćurić, M., Janc, D., Vučković, V. & Kovačević, N. (2009) The impact of the choice of the entire drop size distribution function on cumulonimbus characteristics. *Meteorologische Zeitschrift*, 18(2), 207–222.
- Dai, Q. & Han, D. (2014) Exploration of discrepancy between radar and gauge rainfall estimates driven by wind fields. *Water Resources Research*, 50(11), 8571–8588.
- Dai, Q., Yang, Q., Han, D., Rico-Ramirez, M.A. & Zhang, S. (2019) Adjustment of radar-gauge rainfall discrepancy due to raindrop drift and evaporation using the weather research and forecasting model and dual-polarization radar. *Water Resources Research*, 55(11), 9211–9233.
- Davison, P., Hutchins, M., Anthony, S., Betson, M., Johnson, C. & Lord, E. (2005) The relationship between potentially erosive storm energy and daily rainfall quantity in England and Wales. *Science of the Total Environment*, 344(1–3), 15–25.
- Dee, D.P., Uppala, S.M., Simmons, A., Berrisford, P., Poli, P., Kobayashi, S. et al. (2011) The ERA-Interim reanalysis: configuration and performance of the data assimilation system. *Quarterly Journal of the Royal Meteorological Society*, 137(656), 553–597.
- Dudhia, J. (1989) Numerical study of convection observed during the winter monsoon experiment using a mesoscale two-dimensional model. *Journal of the Atmospheric Sciences*, 46(20), 3077–3107.
- Ek, M., Mitchell, K., Lin, Y., Rogers, E., Grunmann, P., Koren, V. et al. (2003) Implementation of Noah land surface model advances in the National Centers for Environmental Prediction Operational Mesoscale Eta model. *Journal of Geophysical Research: Atmospheres*, 108, 8851.
- Gorgucci, E., Chandrasekar, V., Bringi, V. & Scarchilli, G. (2002) Estimation of raindrop size distribution parameters from polarimetric radar measurements. *Journal of the Atmospheric Sciences*, 59(15), 2373–2384.
- Hamada, A. & Takayabu, Y.N. (2016) Improvements in detection of light precipitation with the global precipitation measurement dual-frequency precipitation radar (GPM DPR). *Journal of Atmospheric and Oceanic Technology*, 33(4), 653–667.
- Han, M., Braun, S.A., Matsui, T. & Williams, C.R. (2013) Evaluation of cloud microphysics schemes in simulations of a winter storm using radar and radiometer measurements. *Journal of Geophysical Research: Atmospheres*, 118(3), 1401–1419.
- Iguchi, T., Seto, S., Meneghini, R., Yoshida, N., Awaka, J., Kubota, T. et al. (2018) *GPM/DPR level-2 algorithm theoretical basis document (version 6)*. Greenbelt, MD: NASA Goddard Space Flight Center.
- Islam, T., Rico-Ramirez, M.A., Thurai, M. & Han, D. (2012) Characteristics of raindrop spectra as normalized gamma distribution from a Joss–Waldvogel disdrometer. *Atmospheric Research*, 108, 57–73.

- Jaffrain, J., Studzinski, A. & Berne, A. (2011) A network of disdrometers to quantify the small-scale variability of the raindrop size distribution. *Water Resources Research*, 47(3), W00H06.
- Jameson, A. & Kostinski, A. (2001a) Reconsideration of the physical and empirical origins of Z–R relations in radar meteorology. *Quarterly Journal of the Royal Meteorological Society*, 127(572), 517–538.
- Jameson, A. & Kostinski, A. (2001b) What is a raindrop size distribution? *Bulletin of the American Meteorological Society*, 82(6), 1169–1178.
- Janjić, Z.I. (1994) The step-mountain eta coordinate model: further developments of the convection, viscous sublayer, and turbulence closure schemes. *Monthly Weather Review*, 122(5), 927–945.
- Ji, L., Chen, H., Li, L., Chen, B., Xiao, X., Chen, M. et al. (2019) Raindrop size distributions and rain characteristics observed by a PARSIVEL disdrometer in Beijing, northern China. *Remote Sensing*, 11(12), 1479.
- Johnson, M., Jung, Y., Dawson, D.T. & Xue, M. (2016) Comparison of simulated polarimetric signatures in idealized supercell storms using two-moment bulk microphysics schemes in WRF. *Monthly Weather Review*, 144(3), 971–996.
- Kain, J.S. (2004) The Kain–Fritsch convective parameterization: an update. *Journal of Applied Meteorology*, 43(1), 170–181.
- Kala, J., Andrys, J., Lyons, T.J., Foster, I.J. & Evans, B.J. (2015) Sensitivity of WRF to driving data and physics options on a seasonal time-scale for the southwest of Western Australia. *Climate Dynamics*, 44(3–4), 633–659.
- Khain, A., Ovtchinnikov, M., Pinsky, M., Pokrovsky, A. & Krugliak, H. (2000) Notes on the state-of-the-art numerical modeling of cloud microphysics. *Atmospheric Research*, 55(3–4), 159–224.
- Khain, A., Lynn, B. & Shpund, J. (2016) High resolution WRF simulations of Hurricane Irene: sensitivity to aerosols and choice of microphysical schemes. *Atmospheric Research*, 167, 129–145.
- Kinnell, P. (2005) Raindrop-impact-induced erosion processes and prediction: a review. *Hydrological Processes*, 19(14), 2815–2844.
- Kirankumar, N., Rao, T.N., Radhakrishna, B. & Rao, D.N. (2008) Statistical characteristics of raindrop size distribution in southwest monsoon season. *Journal of Applied Meteorology and Climatology*, 47(2), 576–590.
- Kumar, P., Kishtawal, C. & Pal, P. (2017) Impact of ECMWF, NCEP, and NCMRWF global model analysis on the WRF model forecast over Indian region. *Theoretical and Applied Climatology*, 127(1–2), 143–151.
- Leinonen, J., Lebsock, M.D., Tanelli, S., Sy, O.O., Dolan, B., Chase, R.J. et al. (2018) Retrieval of snowflake microphysical properties from multifrequency radar observations. *Atmospheric Measurement Techniques*, 11(10), 5471–5488.
- Liao, L., Meneghini, R. & Tokay, A. (2014) Uncertainties of GPM DPR rain estimates caused by DSD parameterizations. *Journal of Applied Meteorology and Climatology*, 53(11), 2524–2537.
- Lim, K.-S.S. & Hong, S.-Y. (2010) Development of an effective double-moment cloud microphysics scheme with prognostic cloud condensation nuclei (CCN) for weather and climate models. *Monthly Weather Review*, 138(5), 1587–1612.
- Lim, Y.S., Kim, J.K., Kim, J.W., Park, B.I. & Kim, M.S. (2015) Analysis of the relationship between the kinetic energy and intensity of rainfall in Daejeon, Korea. *Quaternary International*, 384, 107–117.
- Liu, J., Bray, M. & Han, D. (2013) Exploring the effect of data assimilation by WRF-3DVar for numerical rainfall prediction with different types of storm events. *Hydrological Processes*, 27(25), 3627–3640.
- Lü, G., Batty, M., Strobl, J., Lin, H., Zhu, A.X. & Chen, M. (2019) Reflections and speculations on the progress in geographic information systems (GIS): a geographic perspective. *International Journal of Geographical Information Science*, 33(2), 346–367.
- Mardiana, R., Iguchi, T. & Takahashi, N. (2004) A dual-frequency rain profiling method without the use of a surface reference technique. *IEEE Transactions on Geoscience and Remote Sensing*, 42(10), 2214–2225.
- Meneghini, R., Kumagai, H., Wang, J.R., Iguchi, T. & Kozu, T. (1997) Microphysical retrievals over stratiform rain using measurements from an airborne dual-wavelength radar-radiometer. *IEEE Transactions on Geoscience and Remote Sensing*, 35(3), 487–506.
- Meshesha, D.T., Tsunekawa, A., Tsubo, M., Haregeweyn, N. & Tegegne, F. (2016) Evaluation of kinetic energy and erosivity potential of simulated rainfall using laser precipitation monitor. *Catena*, 137, 237–243.
- Mlawer, E.J., Taubman, S.J., Brown, P.D., Iacono, M.J. & Clough, S. A. (1997) Radiative transfer for inhomogeneous atmospheres: RRTM, a validated correlated-k model for the longwave. *Journal of Geophysical Research: Atmospheres*, 102(D14), 16663–16682.
- Montopoli, M., Marzano, F.S. & Vulpiani, G. (2008) Analysis and synthesis of raindrop size distribution time series from disdrometer data. *IEEE Transactions on Geoscience and Remote Sensing*, 46(2), 466–478.
- Mooney, P.A., Mulligan, F.J. & Fealy, R. (2011) Comparison of ERA-40, ERA-Interim and NCEP/NCAR reanalysis data with observed surface air temperatures over Ireland. *International Journal of Climatology*, 31(4), 545–557.
- Morrison, H., Thompson, G. & Tatarskii, V. (2009) Impact of cloud microphysics on the development of trailing stratiform precipitation in a simulated squall line: comparison of one-and two-moment schemes. *Monthly Weather Review*, 137(3), 991–1007.
- Morrison, H., Milbrandt, J.A., Bryan, G.H., Ikeda, K., Tessendorf, S. A. & Thompson, G. (2015) Parameterization of cloud microphysics based on the prediction of bulk ice particle properties. Part II: case study comparisons with observations and other schemes. *Journal of the Atmospheric Sciences*, 72(1), 312–339.
- Petan, S., Rusjan, S., Vidmar, A. & Mikoš, M. (2010) The rainfall kinetic energy–intensity relationship for rainfall erosivity estimation in the mediterranean part of Slovenia. *Journal of Hydrology*, 391(3–4), 314–321.
- Planche, C., Tridon, F., Banson, S., Thompson, G., Monier, M., Battaglia, A. et al. (2019) On the realism of the rain microphysics representation of a squall line in the WRF model. Part II: sensitivity studies on the rain drop size distributions. *Monthly Weather Review*, 147(8), 2811–2825.
- Prigent, C. (2010) Precipitation retrieval from space: an overview. *Comptes Rendus Geoscience*, 342(4–5), 380–389.
- Radhakrishna, B., Satheesh, S., Narayana Rao, T., Saikranthi, K. & Sunilkumar, K. (2016) Assessment of DSDs of GPM-DPR with ground-based disdrometer at seasonal scale over Gadanki, India. *Journal of Geophysical Research: Atmospheres*, 121(19), 11792–11802.

- Renard, K.G. (1997) *Predicting soil erosion by water: a guide to conservation planning with the Revised Universal Soil Loss Equation (RUSLE)*. Washington, DC: United States Government Printing.
- Rose, C. & Chandrasekar, V. (2006) A GPM dual-frequency retrieval algorithm: DSD profile-optimization method. *Journal of Atmospheric and Oceanic Technology*, 23(10), 1372–1383.
- Seto, S. & Iguchi, T. (2015) Intercomparison of attenuation correction methods for the GPM dual-frequency precipitation radar. *Journal of Atmospheric and Oceanic Technology*, 32(5), 915–926.
- Seto, S., Iguchi, T. & Oki, T. (2013) The basic performance of a precipitation retrieval algorithm for the global precipitation measurement mission's single/dual-frequency radar measurements. *IEEE Transactions on Geoscience and Remote Sensing*, 51(12), 5239–5251.
- Simmons, A. (2006) ERA-Interim: new ECMWF reanalysis products from 1989 onwards. *ECMWF Newsletter*, 110, 25–36.
- Song, Y., Han, D. & Rico-Ramirez, M.A. (2017) High temporal resolution rainfall rate estimation from rain gauge measurements. *Journal of Hydroinformatics*, 19(6), 930–941.
- Thompson, G. & Eidhammer, T. (2014) A study of aerosol impacts on clouds and precipitation development in a large winter cyclone. *Journal of the Atmospheric Sciences*, 71(10), 3636–3658.
- Tokay, A., Petersen, W.A., Gatlin, P. & Wingo, M. (2013) Comparison of raindrop size distribution measurements by collocated disdrometers. *Journal of Atmospheric and Oceanic Technology*, 30(8), 1672–1690.
- Uijlenhoet, R., Steiner, M. & Smith, J.A. (2003) Variability of raindrop size distributions in a squall line and implications for radar rainfall estimation. *Journal of Hydrometeorology*, 4(1), 43–61.
- Ulbrich, C.W. (1983) Natural variations in the analytical form of the raindrop size distribution. *Journal of Climate and Applied Meteorology*, 22(10), 1764–1775.
- Van Dijk, A., Bruijnzeel, L. & Rosewell, C. (2002) Rainfall intensity–kinetic energy relationships: a critical literature appraisal. *Journal of Hydrology*, 261(1–4), 1–23.
- Wang, L., Shi, Z., Wang, J., Fang, N., Wu, G. & Zhang, H. (2014) Rainfall kinetic energy controlling erosion processes and sediment sorting on steep hillslopes: a case study of clay loam soil from the Loess Plateau, China. *Journal of Hydrology*, 512, 168–176.
- Wischmeier, W.H. & Smith, D.D. (1978) *Predicting rainfall erosion losses: a guide to conservation planning*. Washington, DC: Department of Agriculture, Science and Education Administration.
- Yang, Q., Dai, Q., Han, D., Chen, Y. & Zhang, S. (2019) Sensitivity analysis of raindrop size distribution parameterizations in WRF rainfall simulation. *Atmospheric Research*, 228, 1–13.
- Zhu, A., Lu, G., Liu, J., Qin, C. & Zhou, C. (2018) Spatial prediction based on Third Law of Geography. *Annals of GIS*, 24(4), 225–240.

How to cite this article: Zhu, J., Zhang, S., Yang, Q., Shen, Q., Zhuo, L., & Dai, Q. (2021). Comparison of rainfall microphysics characteristics derived by numerical weather prediction modelling and dual-frequency precipitation radar. *Meteorological Applications*, 28(3), e2000. <https://doi.org/10.1002/met.2000>